MATERIALS SCIENCE

Ultrahigh thermal isolation across heterogeneously layered two-dimensional materials

Sam Vaziri[1]*, Eilam Yalon[1]*†, Miguel Muñoz Rojo[1]‡, Saurabh V. Suryavanshi[1], Huairuo Zhang[2,3], Connor J. McClellan[1], Connor S. Bailey[1], Kirby K. H. Smithe[1], Alexander J. Gabourie[1], Victoria Chen[1], Sanchit Deshmukh[1], Leonid Bendersky[3], Albert V. Davydov[3], Eric Pop[1,4,5§]

Heterogeneous integration of nanomaterials has enabled advanced electronics and photonics applications. However, similar progress has been challenging for thermal applications, in part due to shorter wavelengths of heat carriers (phonons) compared to electrons and photons. Here, we demonstrate unusually high thermal isolation across ultrathin heterostructures, achieved by layering atomically thin two-dimensional (2D) materials. We realize artificial stacks of monolayer graphene, MoS_2, and WSe_2 with thermal resistance greater than 100 times thicker SiO_2 and effective thermal conductivity lower than air at room temperature. Using Raman thermometry, we simultaneously identify the thermal resistance between any 2D monolayers in the stack. Ultrahigh thermal isolation is achieved through the mismatch in mass density and phonon density of states between the 2D layers. These thermal metamaterials are an example in the emerging field of phononics and could find applications where ultrathin thermal insulation is desired, in thermal energy harvesting, or for routing heat in ultracompact geometries.

INTRODUCTION

Advanced electronic and photonic devices, like high-electron mobility transistors (*1*), quantum cascade lasers (*2*), and photonic bandgap crystals (*3*), take advantage of the fermionic nature of charge carriers for voltage gating or confinement, and of long photon wavelengths for interference. However, thermal nanoengineering and the emerging field of phononics offer fewer examples, despite high demand in heat management applications (*4*–*6*). This discrepancy is due to the short wavelengths of heat-carrying vibrations in solids, just a few nanometers for the dominant (median) phonon wavelength at room temperature (*7*, *8*), which poses difficulties in nanofabrication at nearly atomic-scale dimensions. The bosonic nature of phonons, which cannot be voltage-gated like the charge carriers, also makes it challenging to actively control heat transport in solids.

Previous efforts to manipulate thermal properties of solids relied on nanolaminate films (*9*) and superlattices (*10*, *11*) to reduce thermal conductivity below that of the constituent materials. These were achieved through structural disordering and high interface density, which introduce additional thermal resistance. Unusually low thermal conductivity was also found in silicon and germanium nanowires, from strong phonon-boundary scattering (*12*, *13*). On the other hand, large thermal conductivities have been achieved in isotopically pure materials, e.g., ^{12}C diamond (*14*) or graphene (*15*), and in the cubic boron arsenide compound through reduced phonon scattering (*16*).

A new frontier is enabled by two-dimensional (2D) materials, which are sub-nanometer thin in single monolayers and thus amenable to control device behavior at atomic length scales (*17*). For example, heterogeneous 2D assemblies have been used for novel tunneling field-effect transistors (*18*) and ultrathin photovoltaics with high efficiency (*19*). Here, we use van der Waals (vdW) assembly of atomically thin 2D layers to achieve unusually high thermal resistance across their heterostructures. Specifically, we show a thermal resistance equivalent to that of ~300-nm SiO_2 across sub–2-nm-thin vdW heterostructures with clean, residue-free interfaces. We also demonstrate the ability of tailoring thermal properties at atomic-scale dimensions, on the order of the phonon wavelength, by layering heterogeneous 2D monolayers with different atomic mass densities and vibrational modes. Such structures form new phononic metamaterials with unusual properties not commonly found in nature. These also represent a unique application of 2D materials and their weak vdW interactions, which can be assembled (here, to block or guide the flow of heat) without the requirement of epitaxially matched interfaces.

RESULTS

Microstructural and optical characteristics

Figure 1A shows the schematic cross-section of a four-layer heterostructure with (from top to bottom) graphene (Gr) on $MoSe_2$, MoS_2, and WSe_2, all on a SiO_2/Si substrate. The Raman laser illustrated is used for simultaneously probing the individual layers in the stack, with single-layer accuracy. All 2D materials are monolayers, separately grown by chemical vapor deposition (CVD) (*20*) and transferred while avoiding polymer and other residues. (Details are provided in Materials and Methods and section S1.) To confirm microstructural, thermal, and electrical uniformity of the heterostructures, we use scanning transmission electron microscopy (STEM), photoluminescence (PL) spectroscopy, Kelvin probe microscopy (KPM), scanning thermal microscopy (SThM), as well as Raman spectroscopy and thermometry.

[1]Department of Electrical Engineering, Stanford University, Stanford, CA 94305, USA. [2]Theiss Research Inc., La Jolla, CA 92037, USA. [3]Materials Science and Engineering Division, National Institute of Standards and Technology (NIST), Gaithersburg, MA 20899, USA. [4]Department of Materials Science and Engineering, Stanford University, Stanford, CA 94305, USA. [5]Precourt Institute for Energy, Stanford University, Stanford, CA 94305, USA.
*These authors contributed equally to this work.
†Present address: Department of Electrical Engineering, Technion-Israel Institute of Technology, Haifa 32000, Israel.
‡Present address: Department of Thermal and Fluid Engineering, University of Twente, 7500 AE Enschede, Netherlands.
§Corresponding author. Email: epop@stanford.edu

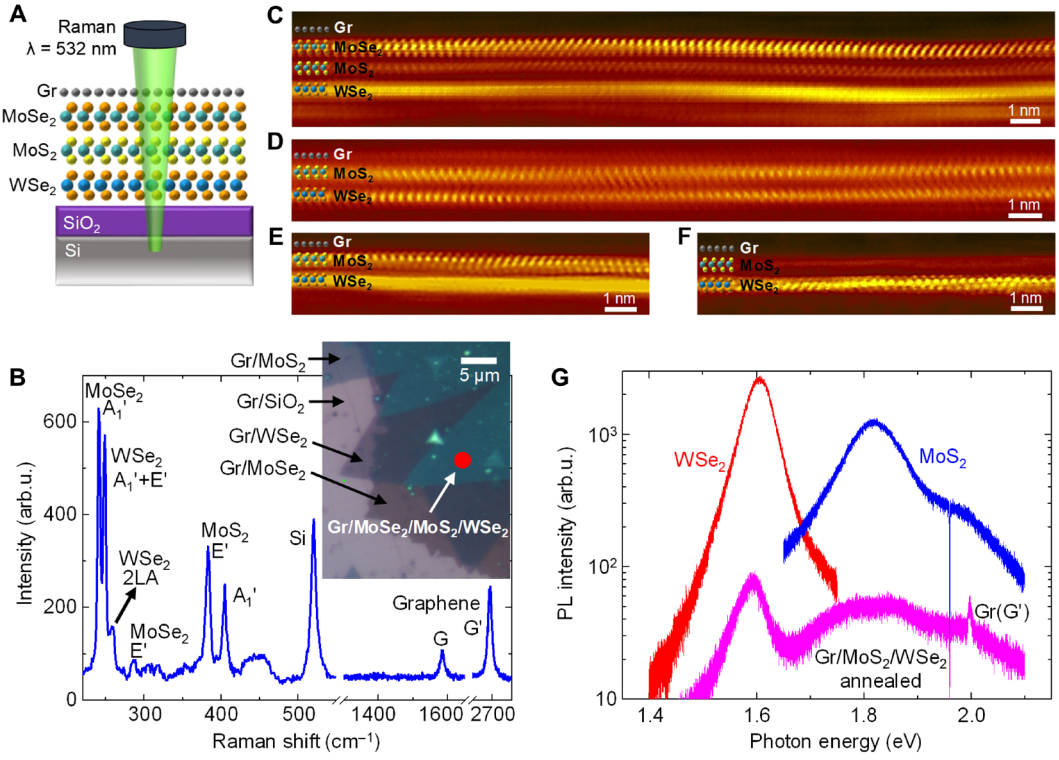

Fig. 1. Optical and STEM characterization of vdW heterostructures. (**A**) Cross-section schematic of Gr/$MoSe_2$/MoS_2/WSe_2 sandwich on SiO_2/Si substrate, with the incident Raman laser. (**B**) Raman spectrum of such a heterostructure at the spot indicated by the red dot in the inset optical image. Raman signatures of all materials in the stack are obtained simultaneously. The graphene Raman spectrum is flattened to exclude the MoS_2 photoluminescence (PL) effect. arb.u., arbitrary units. (**C** to **F**) STEM cross-sectional images of four-layer (C) and three-layer (D to F) heterostructures on SiO_2. In (D), $MoSe_2$ and WSe_2 are approximately aligned along the 1H [100] zone axis, and in (E and F), the layers are misaligned by ~21° with respect to the 1H [100] zone axis. The monolayer graphene on top of each heterostructure is hard to discern due to the much lower atomic number of the carbon atoms. (**G**) PL spectra of monolayer MoS_2, monolayer WSe_2, and a Gr/MoS_2/WSe_2 heterostructure after annealing. The PL is strongly quenched in the heterostructure due to intimate interlayer coupling.

Figure 1B shows the Raman spectrum of such a Gr/$MoSe_2$/MoS_2/WSe_2 heterostructure on SiO_2/Si at the location of the red dot in the inset. It reveals the signature of every 2D material monolayer in the stack, as well as that of the Si substrate. This is a unique strength of the Raman technique, allowing us to identify each material with nonoverlapping Raman modes and to measure its individual temperature. All characteristic Raman peaks of the constituent materials are observed (see Materials and Methods) (*21*), except for the D peak of graphene, indicating negligible disorder.

Figure 1 (C to F) shows cross-sectional atomic-resolution annular dark-field STEM (ADF-STEM) images of our Gr/$MoSe_2$/MoS_2/WSe_2 (Fig. 1C) and Gr/MoS_2/WSe_2 (Fig. 1, D to F) heterostructures with different lattice orientation alignments. Multiple STEM images reveal atomically intimate vdW gaps without contaminants, allowing us to observe the total thickness of these heterostructures, e.g., just below 2 nm for a three-layer stack (also see fig. S2). The interlayer coupling is further confirmed over larger areas by PL spectroscopy (Fig. 1G). The PL signal of individual layers in the heterostructure is substantially quenched (over one order of magnitude) compared to isolated monolayers on the same substrate. This PL quenching is attributed to an interlayer charge transfer process due to intimate interlayer coupling, which becomes even stronger after annealing (see section S3) (*22*).

Electrical characteristics and thermal uniformity

To measure heat flow perpendicular to the atomic planes of the heterostructures, we pattern the stacks in the shape of four-probe electrical devices (see Materials and Methods). The top graphene layer is contacted by Pd electrodes and used as a nearly transparent Joule heater for the Raman thermometry measurements. This electrical heating method enables accurate quantification of the input power (*23*), whereas a purely optical heating method (*24*) would be more challenging without knowing the absorption coefficients of individual layers.

Figure 2 (A and B) displays the schematic of the four-probe measurement and the top view of a test structure, respectively. Figure 2C shows the measured back-gated transfer characteristics of three devices, one with only graphene and two with stacks of Gr/WSe_2 and Gr/$MoSe_2$/WSe_2. These all show the well-known ambipolar behavior of graphene due to the absence of an energy bandgap. They also confirm that current conduction and heating occur in the top graphene layer, its electrical conductivity being orders of magnitude higher than MoS_2 and WSe_2 (see section S6). To demonstrate the uniformity of these devices, we also use KPM and SThM surface characterization. Figure 2D displays KPM measurements taken along the device at various V_{DS}, revealing smooth and linear potential distributions. Figure 2E shows an SThM map of the electrically heated Gr/MoS_2/WSe_2 channel, displaying uniform surface heating with high spatial resolution (see section S4).

Thermometry of the vdW heterostructures

While SThM confirms the surface temperature uniformity of our devices, we used Raman spectroscopy to quantify the temperature of each individual layer. The spectral separation of key Raman

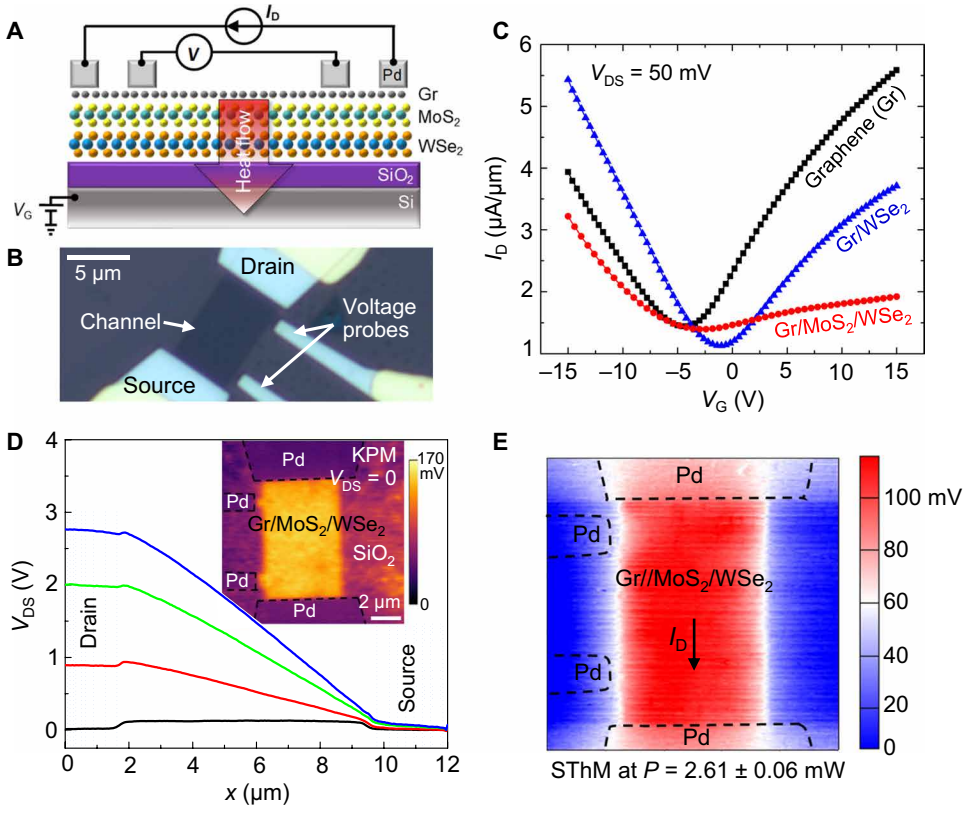

Fig. 2. Electrical and scanning probe characterization. (**A**) Cross-sectional schematic of the test structure showing the four-probe configuration. Electrical current flows in the graphene top layer, and heat dissipates across layers, into the substrate. (**B**) Optical image of a four-probe test structure. Devices are back-gated by the Si substrate through 100-nm SiO_2. (**C**) Measured transfer characteristics of three test structure stacks, Gr/MoS_2/WSe_2, Gr/WSe_2, and Gr-only control devices in vacuum (~10^{-5} torr). All measurements display the ambipolar property of the top graphene channel. (**D**) KPM of an uncapped Gr/MoS_2/WSe_2 heterostructure device. The graph displays the surface potential along the channel (averaged across the channel width) at different bias conditions. The small potential jump near the Pd electrodes represents the relative work function difference (~120 mV). The KPM maps reveal no other heterogeneities in the surface potential, confirming the spatially uniform quality of these devices. The inset shows the zero-bias KPM map. (**E**) SThM thermal map of Gr/MoS_2/WSe_2 heterostructure, here capped with 15-nm Al_2O_3, revealing homogeneous heating across the channel. This confirms the uniformity of the thermal interlayer coupling in the stacks. The device dimensions are the same as in the (D) inset.

features (Fig. 1B) enables sub-nanometer, effectively atomic-scale resolution of the temperature measurement across the 2D stack. We calibrate all temperature-dependent Raman peak shifts (see section S7 for details) and carefully differentiate or rule out nonthermal effects (see Materials and Methods and section S8). We measured three devices of each structure, varying the graphene heater power to 9 mW, while the absorbed laser power was below ~5 μW to avoid optical heating. (All devices have an area of ~40 μm^2, and the laser spot size is ~0.5 μm^2.) Raman peak shifts during electrical heating are converted to temperature rise using the calibration coefficient of each material in the heterostructure (see section S7).

Figure 3A shows the measured temperature rise (ΔT) of each layer, including the Si substrate, as the graphene heater power (P) is ramped up, in a Gr/MoS_2/WSe_2 heterostructure. The slopes of the linear fits for each material indicate the thermal resistance $R_{th} = \Delta T/P$ between that layer and the backside heat sink. Because of uniform heating (Fig. 2E), these thermal resistances are easily analyzed, from bottom to top, normalizing by the channel area, WL. Here, L and W are the channel length and width, much larger than the SiO_2 thickness and the lateral thermal healing length, which is ~0.1 μm (*23*). $R_{th,Si} \approx (WL)^{1/2}/(2k_{Si})$ is the thermal spreading resistance into the Si substrate, yielding $k_{Si} \approx 90$ W m^{-1} K^{-1}, which is the expected thermal conductivity of the highly doped substrate (*23*). The difference between $R_{th,WSe2}$ and $R_{th,Si}$ is the sum of the well-known thermal resistance of 100 nm SiO_2 (*24*) and the thermal boundary resistance (TBR) of the WSe_2/SiO_2 interface. [The TBR of the SiO_2/Si interface is negligible in comparison (*25*).] Then, $R_{th,MoS2} - R_{th,WSe2} = TBR_{MoS2/WSe2}$ and $R_{th,Gr} - R_{th,MoS2} = TBR_{Gr/MoS2}$. Thus, from Fig. 3A, we can extract TBR values for each of the WSe_2/SiO_2, MoS_2/WSe_2, and Gr/MoS_2 interfaces.

We compare the total thermal resistances perpendicular to all heterostructures, measured by Raman and SThM in Fig. 3B. (Unlike Raman, SThM measures only the surface temperature, and its calibration is discussed in section S5.) Knowing the electrical input power, the total thermal resistance between the graphene top layer and the backside heat sink is obtained for all our heterostructures. The excellent agreement between the two thermometry techniques validates the obtained values. The bilayer and trilayer heterostructures on SiO_2 display an effective thermal resistance (normalized by area) in the range of 220 to 280 m^2 K/GW at room temperature, which is equivalent to the thermal resistance (Kapitza length) of 290 to 360 nm of SiO_2. Given the sub–2-nm thickness of these heterostructures (Fig. 1, D to F), they have an effective thermal conductivity of 0.007 to 0.009 W m^{-1} K^{-1} at room temperature, which is approximately a factor of 3 lower than that of ambient air.

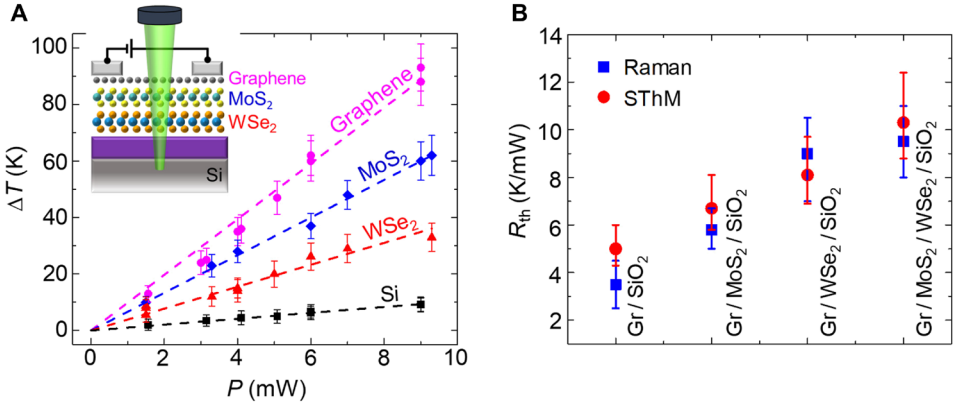

Fig. 3. Thermal resistance of the heterostructures. (**A**) Measured temperature rise ΔT versus electrical input power for each individual layer in a Gr/MoS_2/WSe_2 heterostructure, including the Si substrate, shown in the inset. Graphene (pink circles), MoS_2 (blue diamonds), WSe_2 (red triangles), and Si (black squares). All measurements are carried out at $V_G < 0$ (see section S6). The slopes of the linear fits (dashed lines) represent the thermal resistance R_{th} between each layer and the heat sink. (**B**) Comparison of total thermal resistances (i.e., of the top graphene layer) measured by Raman thermometry and SThM for different vdW heterostructures. The R_{th} values obtained from these two techniques match within the uncertainty of the measurements. All devices have the same active area of ~40 μm^2.

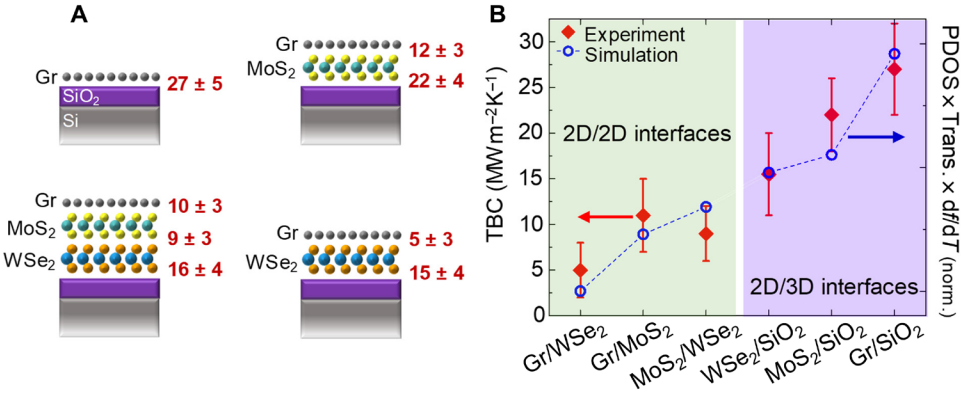

Fig. 4. Summary of TBC trends. (**A**) Schematic of all TBCs measured (in MW m^{-2} K^{-1}) across heterostructures consisting of, clockwise from top left, graphene (Gr), Gr/MoS_2, Gr/WSe_2, and Gr/MoS_2/WSe_2, all on SiO_2/Si substrates. (**B**) Measured TBC values of 2D/2D and 2D/3D (with SiO_2) interfaces (red diamonds, left axis) and the calculated product of phonon density of states (PDOS), phonon transmission, and df/dT (blue circles, right axis). Calculated values are normalized to the minimum achieved for Gr/WSe_2 (see table S2). The dashed line between the simulation symbols is a guide to the eye. Lower TBC is noted at interfaces between 2D/2D materials and those between materials with larger mismatch in mass density. Three devices were measured for each structure, at two or more distinct positions of the Raman laser. No significant TBC variation is seen between samples with different layer (mis)alignment, within the experimental uncertainty. All values are at room temperature.

Understanding the high thermal resistance

We return to the analysis of TBR between layers, ultimately responsible for the very large thermal resistance perpendicular to the heterostructures. Figure 4A summarizes the four measured structures and the thermal boundary conductance (TBC = 1/TBR) of their interfaces. Three devices were measured at multiple positions for each structure, yielding consistent results. The individual 2D layers within the devices were not rotationally aligned, and no significant TBC variation was seen between the different samples within the experimental uncertainty.

These are the first TBC measurements for atomically intimate interfaces between individual monolayers (2D/2D) and the first report of TBC between monolayer WSe_2 and SiO_2. [Previous TBCs between 2D materials had been reported for graphene and MoS_2 on thicker hexagonal boron nitride (h-BN) (*26*–*28*).] Recurring interfaces in different heterostructures (i.e., Gr/MoS_2 and WSe_2/SiO_2) exhibit similar TBC, confirming the quality of the interfaces and the reproducibility of the measurements. The TBCs for Gr/SiO_2 and MoS_2/SiO_2 interfaces are in agreement with previous studies (*23*, *24*, *29*). The TBC of the monolayer WSe_2/SiO_2 interface is lower than for few-layer WSe_2/SiO_2 (*30*), which is not unexpected, because the monolayer has fewer flexural phonon modes available for transmission (*31*).

In general, we find that 2D/2D interface TBC is lower than 2D interface TBC with the three-dimensional (3D) SiO_2 substrate (Fig. 4B). In addition, the lowest TBC recorded belongs to Gr/WSe_2, the 2D/2D interface with the largest areal mass density mismatch. We explain these trends using Landauer's formalism (see section S9 for details), wherein the TBC across the interface is proportional to the product of the phonon density of states (PDOS) overlap, the transmission coefficient, and df/dT, where f is Bose-Einstein distribution. Here, we consider the PDOS for flexural out-of-plane (ZA) phonons, which have been shown to dominate cross-plane heat conduction in 2D materials (*32*). For the SiO_2 substrate, we consider the typical longitudinal acoustic (LA) and transverse acoustic (TA) phonon branches.

The phonon transmission at the interface is obtained from the acoustic mismatch model (AMM) as the ratio of mass density of the two materials (*33*). The AMM is a good approximation because the

vdW interfaces are nearly perfect, with any surface asperities (e.g., few dangling bonds) being much smaller than the phonon wavelengths. As shown in Fig. 4B, the TBC trends are captured by our simple model of heat flow across the interfaces (additional details are provided in the Supplementary Materials). These results also support the dominant role of ZA phonons for cross-plane heat transport in 2D material vdW heterostructures. Thus, higher (or lower) interfacial heat transmission of 2D materials could be obtained by maximizing (or minimizing) the PDOS overlap and reducing (or increasing) the areal mass density mismatch.

CONCLUSIONS

The knowledge gained in this study will enable the realization of atomically tailored thermal interfaces, in a manner similar to how energy band (mis)alignments are tailored for modulation doping (*1*) and optoelectronic devices (*2*). We have demonstrated the ability to engineer extremely insulating thermal metamaterials, with properties not otherwise available in nature, and to measure their temperature with atomic layer precision. These heterostructures are an example in the emerging field of phononics, manipulating the thermal properties of solids at length scales comparable to the phonon wavelengths. Such layered 2D materials are promising as ultralight and compact heat shields, e.g., directing heat away from hot spots in electronics. They could also be used to improve the efficiency of thermoelectric energy harvesters (*5*) or that of thermally activated devices like phase-change memories (*34*), if the cross-plane electrical conductivity can be simultaneously optimized.

MATERIALS AND METHODS

2D layer growth

Monolayer graphene was grown on Cu foil (99.8%, Alfa Aesar) using an Aixtron Black Magic Pro 4-inch CVD system. Before growth, the Cu surface oxide was selectively etched in HCl–deionized water (DIW) (1:2) solution for 10 min. Then, the Cu foil was annealed at 1050°C in Ar/H_2 flow for 30 min. The growth was done at 1050°C under a flow rate of 10 standard cubic centimeters per minute (sccm) CH_4 and 30 sccm H_2 for 15 min. Monolayer MoS_2, $MoSe_2$, and WSe_2 were CVD-grown directly on SiO_2/p^+-Si (1 to 5 mΩ·cm) substrates at 800° to 900°C using S or Se solid sources with solid MoO_3 or WO_3 in a 2-inch tube furnace (*20*) under a flow rate of 10 sccm Ar for MoS_2 and 25/5 sccm Ar/H_2 for the selenides. To promote the growth, perylene-3,4,9,10-tetracarboxylic acid tetrapotassium salt (PTAS) was used as a seed for the lateral epitaxial growth.

Fabrication

The multiple transfer process was done using a bilayer polymer stack of poly(methyl methacrylate) (PMMA) (950,000, 2.5% mass in chlorobenzene) and polystyrene (PS). PMMA was spin-coated on graphene (on Cu substrate) at 3500 rpm for 1 min followed by baking on a hot plate at 150°C for 45 s. Then, PS was spin-coated at 3000 rpm for 1 min followed by baking on a hot plate at 85°C for 5 min. The Cu substrate was etched in $FeCl_3$, and then the polymer/graphene stack was rinsed using diluted HCl and DIW. Subsequently, the polymer/graphene stack was transferred, for instance, onto MoS_2 on SiO_2 substrate followed by baking at 60°, 90°, and 135°C for 30, 15, and 1 min, respectively. (We have found this gradual baking to remove bubble formation.) The polymer-supporting layer was removed in toluene before repeating the same procedure to transfer the graphene/MoS_2 stack onto the next substrate, etc. The transition metal dichalcogenide (TMD) monolayers were delaminated from the SiO_2 growth substrate in 1 M NaOH solution. After formation of the target vdW heterostructures, the samples were annealed at 275°C in vacuum to remove residual water between the layers and promote interlayer coupling (*22*).

The heterostructure channels were defined using electron beam lithography and O_2 plasma reactive ion etching. Subsequently, photolithography and liftoff were applied to make 50-nm Pd metal contacts to the top graphene channel. Then, a similar process was repeated to fabricate Ti/Au (5 nm/65 nm) electrical measurement pads. Last, the devices were capped with 15-nm atomic layer deposition of Al_2O_3, which induces *n*-type doping and protects the graphene channel from the ambient. All devices had a four-probe structure with identical dimensions of the channel length, $L = 8$ μm, and width, $W = 5$ μm. The four-probe structure was used to accurately identify the electrical input power density. Before Raman thermometry, electrical measurements were carried out in air and at room temperature using a Keithley 4200 instrument.

TEM sample preparation

FEI Nova NanoLab 600 dual-beam scanning electron microscopy (SEM) and focused ion beam (FIB) system were used to prepare cross-sectional TEM samples. A 1-μm-thick carbon layer was initially deposited (by electron beam–induced deposition) on top of the device to protect the sample surface, followed by 2-μm ion beam–induced Pt deposition. To reduce Ga ions damage, in the final step of FIB preparation, the TEM samples were thinned with 2-kV Ga ions using a low beam current of 29 pA and a small incident angle of 3°. The surface damage of the samples was further reduced using a precision ion polishing system (Gatan PIPS II) with 0.1-kV Ar ions.

STEM characterization

An FEI Titan 80-300 STEM/TEM equipped with a monochromator and a probe spherical aberration corrector was used to acquire atomic-resolution STEM images. Atomic-resolution ADF-STEM images were acquired with an operating voltage of 300 kV, a probe convergence angle of 24 mrad, and a collection angle of 34 to 195 mrad.

Scanning probe characterization

SThM and KPM were performed using an MFP-3D infinity atomic force microscope (AFM) from Asylum Research with an added thermal module from Anasys Instruments. The SThM used a thermoresistor probe from Anasys Instruments, which consists of a thin Pd line on SiN. We used the probes in contact mode to sense the temperature at the surface of the heterostructures. The KPM was carried out with a metal-coated tip from Asylum Research in noncontact mode using amplitude modulation detection. In both SThM and KPM, the graphene top layer was electrically contacted using the AFM probe station from Asylum Research and a Keithley 4200 instrument.

Raman and PL measurements

Raman and PL spectroscopy were carried out using a Horiba LabRAM instrument with a 532-nm laser and 100× long working distance objective with a numerical aperture (NA) of 0.6. Step sizes in the Raman maps varied between 0.4 and 0.6 μm, and the acquisition time of each device thermal map was ~20 to 30 min. The laser spot radius was ~0.4 μm, and the absorbed laser power was <5 μW to

avoid laser heating in excess of the electrical heating and to maintain negligible photocurrent. The Raman spectra of the four-layer heterostructure of Gr/$MoSe_2$/MoS_2/WSe_2 (Fig. 1B) showed peaks at 241.5 and 404.6 cm^{-1} corresponding to out-of-plane A_1' modes for $MoSe_2$ and MoS_2, respectively. The in-plane E′ modes for $MoSe_2$ and MoS_2 were represented by the peaks at 286.5 and 383.1 cm^{-1}, respectively. Monolayer WSe_2 showed the characteristic degenerate peak at 249.4 cm^{-1}, which included both A_1' and E′, while the 2LA peak was at 259.3 cm^{-1}. Furthermore, the G and G′ (sometimes called 2D) peaks of monolayer graphene were at 1585.3 and 2690.5 cm^{-1}, respectively. We used the graphene G peak and the TMD out-of-plane modes for thermometry because they were less sensitive to strain.

For temperature-dependent Raman shift calibration, we used a Linkam THMS600 stage and carefully differentiated effects of strain (e.g., during the calibration on hot stage) and shifts due to electrical bias (gating effect from the substrate), following the calibration procedure outlined in section S7. The obtained Raman temperature maps were uniform (see section S6), similar to the SThM measurements shown in section S4. The uniform heating in the channel indicated that there was no measurable nonuniform doping or pinch-off, which simplified the extraction of interlayer TBC. Changes in the measured current along the graphene channel during mapping were smaller than 5%. All thermometry measurements were performed in ambient and at room temperature.

SUPPLEMENTARY MATERIALS

Supplementary material for this article is available at http://advances.sciencemag.org/cgi/content/full/5/8/eaax1325/DC1

Section S1. Multiple transfer technique
Section S2. Atomic-resolution ADF-STEM
Section S3. PL quenching in 2D heterostructures
Section S4. SThM thermal maps
Section S5. SThM temperature calibration
Section S6. Raman temperature maps
Section S7. Temperature-dependent Raman coefficients
Section S8. Non–temperature-related Raman peak shifts
Section S9. Thermal transport modeling and analysis
Fig. S1. Transfer process and optical images.
Fig. S2. Atomic-resolution ADF-STEM images.
Fig. S3. PL quenching.
Fig. S4. Uniform heating maps.
Fig. S5. SThM calibration by metal line heaters.
Fig. S6. Raman maps.
Fig. S7. Temperature-dependent Raman coefficients.
Fig. S8. Raman shift dependence on doping and electrical gating.
Fig. S9. PDOS overlap.
Table S1. Material parameters.
Table S2. TBC comparison.
References (*35*–*55*)

REFERENCES AND NOTES

1. T. Mimura, S. Hiyamizu, T. Fujii, K. Nanbu, A new field-effect transistor with selectively doped GaAs/n-$Al_xGa_{1-x}As$ heterojunctions. *Jpn. J. Appl. Phys.* **19**, L225–L227 (1980).
2. J. Faist, F. Capasso, D. L. Sivco, C. Sirtori, A. L. Hutchinson, A. Y. Cho, Quantum cascade laser. *Science* **264**, 553–556 (1994).
3. E. Yablonovitch, Photonic band-gap crystals. *J. Phys. Condens. Matter* **5**, 2443–2460 (1993).
4. M. Maldovan, Sound and heat revolutions in phononics. *Nature* **503**, 209–217 (2013).
5. M. S. Dresselhaus, G. Chen, M. Y. Tang, R. G. Yang, H. Lee, D. Z. Wang, Z. F. Ren, J.-P. Fleurial, P. Gogna, New directions for low-dimensional thermoelectric materials. *Adv. Mater.* **19**, 1043–1053 (2007).
6. P. Ball, Computer engineering: Feeling the heat. *Nature* **492**, 174–176 (2012).
7. J. Mair, R. Anufriev, R. Yanagisawa, A. Ramiere, S. Volz, M. Nomura, Heat conduction tuning by wave nature of phonons. *Sci. Adv.* **3**, e1700027 (2017).
8. A. Sood, F. Xiong, S. Chen, R. Cheaito, F. Lian, M. Asheghi, Y. Cui, D. Donadio, K. E. Goodson, E. Pop, Quasi-ballistic thermal transport across MoS_2 thin films. *Nano Lett.* **19**, 2434–2442 (2019).
9. R. M. Costescu, D. G. Cahill, F. H. Fabreguette, Z. A. Sechrist, S. M. George, Ultra-low thermal conductivity in W/Al_2O_3 nanolaminates. *Science* **303**, 989–990 (2004).
10. C. Chiritescu, D. G. Cahill, N. Nguyen, D. Johnson, A. Bodapati, P. Keblinski, P. Zschack, Ultralow thermal conductivity in disordered, layered WSe_2 crystals. *Science* **315**, 351–353 (2007).
11. Z. Li, S. Bauers, N. Poudel, D. Hamann, X. Wang, D. S. Choi, K. Esfarjani, L. Shi, D. C. Johnson, S. B. Cronin, Cross-plane seebeck coefficient measurement of Misfit layered compounds $(SnSe)_n(TiSe_2)_n$, (n=1,3,4,5). *Nano Lett.* **17**, 1978–1986 (2017).
12. M. G. Ghossoub, K. V. Valavala, M. Seong, B. Azeredo, K. Hsu, J. S. Sadhu, P. K. Singh, S. Sinha, Spectral phonon scattering from sub-10 nm surface roughness wavelengths in metal-assisted chemically etched Si nanowires. *Nano Lett.* **13**, 1564–1571 (2013).
13. P. N. Martin, Z. Aksamija, E. Pop, U. Ravaioli, Reduced thermal conductivity in nanoengineered rough Ge and GaAs nanowires. *Nano Lett.* **10**, 1120–1124 (2010).
14. T. R. Anthony, W. F. Banholzer, J. F. Fleischer, L. Wei, P. K. Kuo, R. L. Thomas, R. W. Pryor, Thermal diffusivity of isotopically enriched ^{12}C diamond. *Phys. Rev. B* **42**, 1104–1111 (1990).
15. S. Chen, Q. Wu, C. Mishra, J. Kang, H. Zhang, K. Cho, W. Cai, A. A. Balandin, R. S. Ruoff, Thermal conductivity of isotopically modified graphene. *Nat. Mater.* **11**, 203–207 (2012).
16. S. Li, Q. Zheng, Y. Lv, X. Liu, X. Wang, P. Y. Huang, D. G. Cahill, B. Lv, High thermal conductivity in cubic boron arsenide crystals. *Science* **361**, 579–581 (2018).
17. K. S. Novoselov, A. Mishchenko, A. Carvalho, A. H. C. Neto, 2D materials and van der Waals heterostructures. *Science* **353**, aac9439 (2016).
18. L. Britnell, R. V. Gorbachev, R. Jalil, B. D. Belle, F. Schedin, A. Mishchenko, T. Georgiou, M. I. Katsnelson, L. Eaves, S. V. Morozov, N. M. R. Peres, J. Leist, A. K. Geim, K. S. Novoselov, L. A. Ponomarenko, Field-effect tunneling transistor based on vertical graphene heterostructures. *Science* **335**, 947–950 (2012).
19. W. Zhang, Q. Wang, Y. Chen, Z. Wang, A. T. S. Wee, Van der Waals stacked 2D layered materials for optoelectronics. *2D Mater.* **3**, 022001 (2016).
20. K. K. H. Smithe, C. D. English, S. V. Suryavanshi, E. Pop, Intrinsic electrical transport and performance projections of synthetic monolayer MoS_2 devices. *2D Mater.* **4**, 011009 (2017).
21. X. Zhang, X.-F. Qiao, W. Shi, J.-B. Wu, D.-S. Jiang, P.-H. Tan, Phonon and Raman scattering of two-dimensional transition metal dichalcogenides from monolayer, multilayer to bulk material. *Chem. Soc. Rev.* **44**, 2757–2785 (2015).
22. M.-H. Chiu, M.-Y. Li, W. Zhang, W.-T. Hsu, W.-H. Chang, M. Terrones, H. Terrones, L.-J. Li, Spectroscopic signatures for interlayer coupling in MoS_2-WSe_2 van der Waals stacking. *ACS Nano* **8**, 9649–9656 (2014).
23. E. Yalon, C. J. McClellan, K. K. H. Smithe, M. Muñoz Rojo, R. L. Xu, S. V. Suryavanshi, A. J. Gabourie, C. M. Neumann, F. Xiong, A. B. Farimani, E. Pop, Energy dissipation in monolayer MoS_2 Electronics. *Nano Lett.* **17**, 3429–3433 (2017).
24. E. Yalon, Ö. B. Aslan, K. K. H. Smithe, C. J. McClellan, S. V. Suryavanshi, F. Xiong, A. Sood, C. M. Neumann, X. Xu, K. E. Goodson, T. F. Heinz, E. Pop, Temperature-dependent thermal boundary conductance of monolayer MoS_2 by Raman thermometry. *ACS Appl. Mater. Interfaces* **9**, 43013–43020 (2017).
25. J. Kimling, A. Philippi-Kobs, J. Jacobsohn, H. P. Oepen, D. G. Cahill, Thermal conductance of interfaces with amorphous SiO_2 measured by time-resolved magneto-optic Kerr-effect thermometry. *Phys. Rev. B* **95**, 184305 (2017).
26. C.-C. Chen, Z. Li, L. Shi, S. B. Cronin, Thermal interface conductance across a graphene/hexagonal boron nitride heterojunction. *Appl. Phys. Lett.* **104**, 081908 (2014).
27. D. Kim, H. Kim, W. S. Yun, K. Watanabe, T. Taniguchi, H. Rho, M.-H. Bae, Energy dissipation mechanism revealed by spatially resolved Raman thermometry of graphene/hexagonal boron nitride heterostructure devices. *2D Mater.* **5**, 025009 (2018).
28. Y. Liu, Z.-Y. Ong, J. Wu, Y. Zhao, K. Watanabe, T. Taniguchi, D. Chi, G. Zhang, J. T. L. Thong, C.-W. Qiu, K. Hippalgaonkar, Thermal conductance of the 2D MoS_2/h-BN and graphene/h-BN interfaces. *Sci. Rep.* **7**, 43886 (2017).
29. M. Freitag, M. Steiner, Y. Martin, V. Perebeinos, Z. Chen, J. C. Tsang, P. Avouris, Energy dissipation in graphene field-effect transistors. *Nano Lett.* **9**, 1883–1888 (2009).
30. A. Behranginia, Z. Hemmat, A. K. Majee, C. J. Foss, P. Yasaei, Z. Aksamija, A. Salehi-Khojin, Power dissipation of WSe_2 field-effect transistors probed by low-frequency Raman thermometry. *ACS Appl. Mater. Interfaces* **10**, 24892–24898 (2018).
31. Z.-Y. Ong, Thickness-dependent Kapitza resistance in multilayered graphene and other two-dimensional crystals. *Phys. Rev. B* **95**, 155309 (2017).
32. Z.-Y. Ong, B. Qiu, S. Xu, X. Ruan, E. Pop, Flexural resonance mechanism of thermal transport across graphene-SiO_2 interfaces. *J. Appl. Phys.* **123**, 115107 (2018).
33. W. A. Little, The transport of heat between dissimilar solids at low temperatures, in *From High-Temperature Superconductivity to Microminiature Refrigeration*, B. Cabrera, H. Gutfreund, V. Kresin, Eds. (Springer, 1996), pp. 15–30.
34. C. M. Neumann, K. L. Okabe, E. Yalon, R. W. Grady, H.-S. P. Wong, E. Pop, Engineering thermal and electrical interface properties of phase change memory with monolayer MoS_2. *Appl. Phys. Lett.* **114**, 082103 (2019).

35. X. Hong, J. Kim, S.-F. Shi, Y. Zhang, C. Jin, Y. Sun, S. Tongay, J. Wu, Y. Zhang, F. Wang, Ultrafast charge transfer in atomically thin MoS_2/WS_2 heterostructures. *Nat. Nanotechnol.* **9**, 682–686 (2014).
36. B. Peng, G. Yu, X. Liu, B. Liu, X. Liang, L. Bi, L. Deng, T. C. Sum, K. P. Loh, Ultrafast charge transfer in MoS_2/WSe_2 p-n heterojunction. *2D Mater.* **3**, 025020 (2016).
37. C. H. Lui, Z. P. Ye, C. Ji, K.-C. Chiu, C.-T. Chou, T. I. Andersen, C. Means-Shively, H. Anderson, J.-M. Wu, T. Kidd, Y.-H. Lee, R. He, Observation of interlayer phonon modes in van der Waals heterostructures. *Phys. Rev. B* **91**, 165403 (2015).
38. H. Li, J.-B. Wu, F. Ran, M.-L. Lin, X.-L. Liu, Y. Zhao, X. Lu, Q. Xiong, J. Zhang, W. Huang, H. Zhang, P.-H. Tan, Interfacial interactions in van der Waals heterostructures of MoS_2 and graphene. *ACS Nano* **11**, 11714–11723 (2017).
39. S. Gomès, A. Assy, P.-O. Chapuis, Scanning thermal microscopy: A review. *Phys. Status Solidi A* **212**, 477–494 (2015).
40. E. Puyoo, S. Grauby, J.-M. Rampnoux, E. Rouviere, S. Dilhaire, Thermal exchange radius measurement: Application to nanowire thermal imaging. *Rev. Sci. Instrum.* **81**, 073701 (2010).
41. S. Deshmukh, M. M. Rojo. E. Yalon, S. Vaziri, E. Pop, Probing self-heating in RRAM devices by sub-100 nm spatially resolved thermometry, in *76th IEEE Device Research Conference* (IEEE, 2018).
42. H. Li, Q. Zhang, C. C. R. Yap, B. K. Tay, T. H. T. Edwin, A. Olivier, D. Baillargeat, From bulk to monolayer MoS_2: Evolution of Raman scattering. *Adv. Funct. Mater.* **22**, 1385–1390 (2012).
43. A. C. Ferrari, D. M. Basko, Raman spectroscopy as a versatile tool for studying the properties of graphene. *Nat. Nanotechnol.* **8**, 235–246 (2013).
44. J. E. Lee, G. Ahn, J. Shim, Y. S. Lee, S. Ryu, Optical separation of mechanical strain from charge doping in graphene. *Nat. Commun.* **3**, 1024 (2012).
45. X. Hu, P. Yasaei, J. Jokisaari, S. Öğüt, A. Salehi-Khojin, R. F. Klie, Mapping thermal expansion coefficients in freestanding 2D materials at the nanometer scale. *Phys. Rev. Lett.* **120**, 55902 (2018).
46. J.-H. Zhao, T. Ryan, P. S. Ho, A. J. McKerrow, W.-Y. Shih, Measurement of elastic modulus, Poisson ratio, and coefficient of thermal expansion of on-wafer submicron films. *J. Appl. Phys.* **85**, 6421–6424 (1999).
47. C. Rice, R. J. Young, R. Zan, U. Bangert, D. Wolverson, T. Georgiou, R. Jalil, K. S. Novoselov, Raman-scattering measurements and first-principles calculations of strain-induced phonon shifts in monolayer MoS_2. *Phys. Rev. B* **87**, 81307 (2013).
48. H. Sahin, S. Tongay, S. Horzum, W. Fan, J. Zhou, J. Li, J. Wu, F. M. Peeters, Anomalous Raman spectra and thickness-dependent electronic properties of WSe_2. *Phys. Rev. B* **87**, 165409 (2013).
49. S. B. Desai, G. Seol, J. S. Kang, H. Fang, C. Battaglia, R. Kapadia, J. W. Ager, J. Guo, A. Javey, Strain-induced indirect to direct bandgap transition in multilayer WSe_2. *Nano Lett.* **14**, 4592–4597 (2014).
50. A. Das, S. Pisana, B. Chakraborty, S. Piscanec, S. K. Saha, U. V. Waghmare, K. S. Novoselov, H. R. Krishnamurthy, A. K. Geim, A. C. Ferrari, A. K. Sood, Monitoring dopants by Raman scattering in an electrochemically top-gated graphene transistor. *Nat. Nanotechnol.* **3**, 210–215 (2008).
51. B. N. J. Persson, A. I. Volokitin, H. Ueba, Phononic heat transfer across an interface: Thermal boundary resistance. *J. Phys. Condens. Matter* **23**, 045009 (2011).
52. Z. Li, Y. Liu, L. Lindsay, Y. Xu, W. Duan, E. Pop, Size dependence and ballistic limits of thermal transport in anisotropic layered two-dimensional materials. arXiv:1711.02772 [cond-mat.mes-hall] (2017).
53. J.-W. Jiang, Z. Qi, H. S. Park, T. Rabczuk, Elastic bending modulus of single-layer molybdenum disulfide (MoS_2): Finite thickness effect. *Nanotechnology* **24**, 435705 (2013).
54. K. Lai, W.-B. Zhang, F. Zhou, F. Zeng, B.-Y. Tang, Bending rigidity of transition metal dichalcogenide monolayers from first-principles. *J. Phys. D Appl. Phys.* **49**, 185301 (2016).
55. W.-X. Zhou, K.-Q. Chen, First-principles determination of ultralow thermal conductivity of monolayer WSe_2. *Sci. Rep.* **5**, 15070 (2015).

Acknowledgments: We thank Z.-Y. Ong for fruitful discussions regarding the modeling. **Funding:** Device fabrication and measurements were performed in part at the Stanford Nanofabrication Facility (SNF) and the Stanford Nano Shared Facilities (SNSF), which received funding from the National Science Foundation (NSF) as part of National Nanotechnology Coordinated Infrastructure Award ECCS-1542152. This work was supported in part by ASCENT, one of six centers in JUMP, a Semiconductor Research Corporation (SRC) program sponsored by DARPA, in part by Air Force Office of Scientific Research (AFOSR) grant FA9550-14-1-0251, NSF EFRI 2-DARE grant 1542883, and the Stanford SystemX Alliance. The Knut and Alice Wallenberg Foundation partially supported S.V. through a postdoctoral fellowship. A.J.G. acknowledged support from the NDSEG Fellowship. K.K.H.S. acknowledged partial support from the Stanford Graduate Fellowship (SGF) program and NSF Graduate Research Fellowship under grant no. DGE-114747. H.Z. acknowledged support from the U.S. Department of Commerce, NIST under award 70NANB17H249. C.S.B. acknowledged support from the NSF Graduate Research Fellowship. Certain commercial equipment, instruments, or materials are identified in this paper to specify the experimental procedure adequately. Such identification is not intended to imply recommendation or endorsement by the National Institute of Standards and Technology (NIST), nor is it intended to imply that the materials or equipment identified are necessarily the best available for the purpose. **Author contributions:** S.V., E.Y., and E.P conceived the experiments and wrote the manuscript with input from all authors. C.S.B., K.K.H.S., and S.V. grew the TMDs and graphene. S.V. developed the transfer process and made the heterostructures. S.V., C.J.M., and V.C. fabricated the devices. S.V. performed electrical and PL characterizations. E.Y. and S.V. conducted Raman characterization and thermometry. E.Y. analyzed the Raman data. M.M.R. performed AFM, KPM, and SThM. M.M.R., E.Y., and S.V. analyzed the SThM results. S.D. and S.V. fabricated the SThM calibration samples. S.D., M.M.R., and E.Y. performed calibration analysis to extract conversion factors. S.V.S., A.J.G., and S.V. developed the TBC model and performed the simulations, with input from E.P. H.Z. conducted TEM sample FIB preparation and performed atomic-resolution STEM imaging, STEM EDS, and EELS spectrum-imaging measurements. H.Z., L.B., and A.V.D. conducted the STEM data analysis. **Competing interests:** The authors declare that they have no competing interests. **Data and materials availability:** All data needed to evaluate the conclusions in the paper are present in the paper and/or the Supplementary Materials. Additional data related to this paper may be requested from the authors.

Submitted 25 February 2019
Accepted 10 July 2019
Published 16 August 2019
10.1126/sciadv.aax1325

Citation: S. Vaziri, E. Yalon, M. Muñoz Rojo, S. V. Suryavanshi, H. Zhang, C. J. McClellan, C. S. Bailey, K. K. H. Smithe, A. J. Gabourie, V. Chen, S. Deshmukh, L. Bendersky, A. V. Davydov, E. Pop, Ultrahigh thermal isolation across heterogeneously layered two-dimensional materials. *Sci. Adv.* **5**, eaax1325 (2019).

ScienceAdvances

Ultrahigh thermal isolation across heterogeneously layered two-dimensional materials

Sam Vaziri, Eilam Yalon, Miguel Muñoz Rojo, Saurabh V. Suryavanshi, Huairuo Zhang, Connor J. McClellan, Connor S. Bailey, Kirby K. H. Smithe, Alexander J. Gabourie, Victoria Chen, Sanchit Deshmukh, Leonid Bendersky, Albert V. Davydov and Eric Pop

Sci Adv **5** (8), eaax1325.
DOI: 10.1126/sciadv.aax1325

Science Advances
AAAS

advances.sciencemag.org/cgi/content/full/5/8/eaax1325/DC1

Supplementary Materials for

Ultrahigh thermal isolation across heterogeneously layered two-dimensional materials

Sam Vaziri, Eilam Yalon, Miguel Muñoz Rojo, Saurabh V. Suryavanshi, Huairuo Zhang, Connor J. McClellan, Connor S. Bailey, Kirby K. H. Smithe, Alexander J. Gabourie, Victoria Chen, Sanchit Deshmukh, Leonid Bendersky, Albert V. Davydov, Eric Pop*

*Corresponding author. Email: epop@stanford.edu

Published 16 August 2019, *Sci. Adv.* **5**, eaax1325 (2019)
DOI: 10.1126/sciadv.aax1325

This PDF file includes:

Section S1. Multiple transfer technique

Figure S1A shows the heterostructure fabrication process flow. The process starts with transferring graphene, grown by chemical vapor deposition (CVD) on copper, onto the second two-dimensional (2D) material which is, in this example, CVD-grown $MoSe_2$ on SiO_2 as shown in fig. S1A, I to III. This graphene sheet will be the topmost (first) layer of the final van der Waals (vdW) heterostructure. The top graphene layer acts as an optically transparent electrical heater for Raman thermometry of the heterostructures. After removing the polymer followed by annealing, the sample is coated with another layer of transfer support polymer. Then, the stack of polymer/Gr/$MoSe_2$ is delaminated from the SiO_2/Si substrate using DI water or diluted NaOH and transferred onto the third 2D material which is CVD-grown MoS_2 in this example (fig. S1A, IV and V). The same procedure can be repeated to form the target stack (fig. S1A, VI). In this method, the transfer-support polymer layer is only in contact with the top surface of the graphene layer, leaving all the interfaces below polymer-free. Figures S1B,C,D show optical images of the fabricated heterostructures.

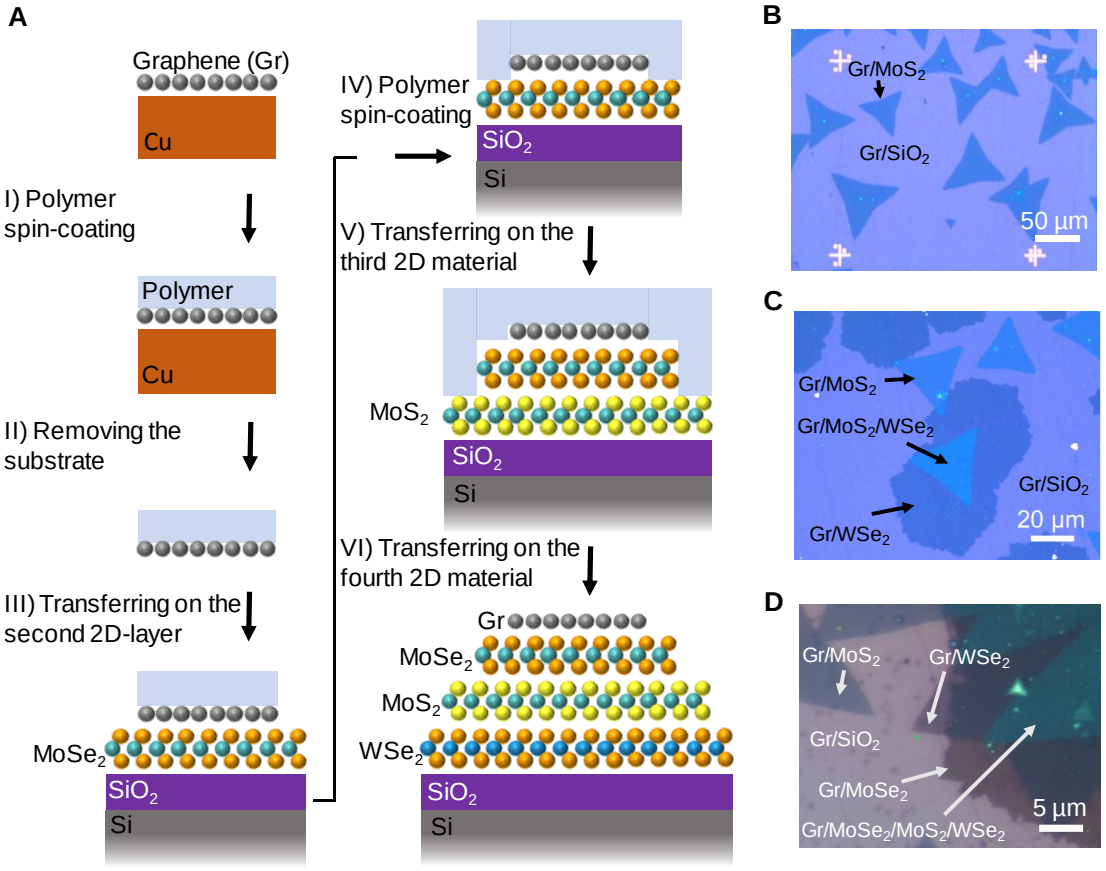

Fig. S1. Transfer process and optical images. (**A**) Schematic of the multiple-transfer process flow to fabricate a Gr/$MoSe_2$/MoS_2/WSe_2 heterostructure on SiO_2/Si substrate. Optical images of (**B**) Gr/MoS_2, (**C**) Gr/MoS_2/WSe_2, and (**D**) Gr/$MoSe_2$/MoS_2/WSe_2 on SiO_2/Si substrates.

Section S2. Atomic-resolution ADF-STEM

The individual 2D monolayers have random lattice orientation and alignment with respect to each other in the vdW heterostructures. This makes it challenging to simultaneously attain atomically sharp transmission electron microscopy (STEM) images of all layers in the stack.

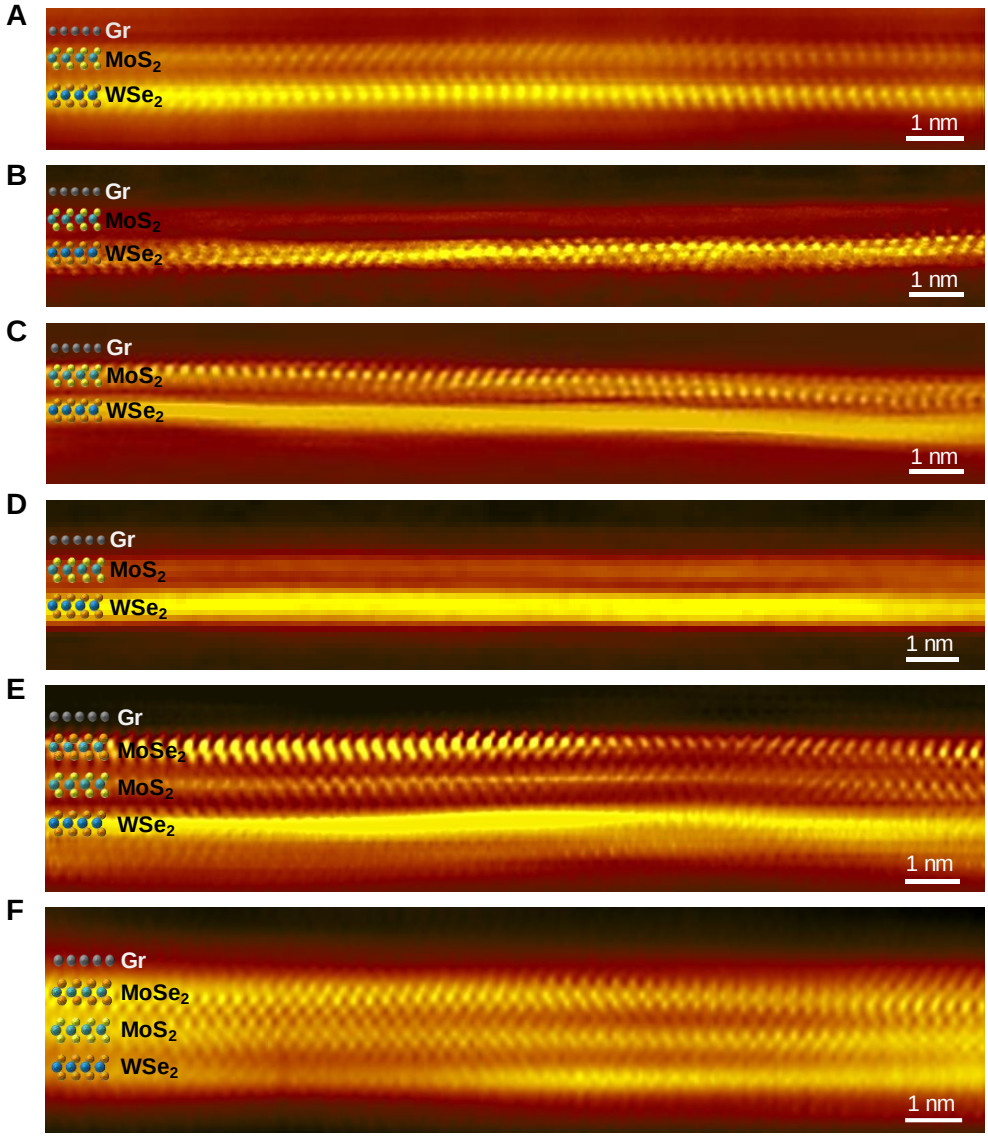

Fig. S2. Atomic-resolution ADF-STEM images. (**A-D**) STEM images of Gr/MoS_2/WSe_2 heterostructures. (A) MoS_2 and WSe_2 are slightly misaligned with respect to each other along the 1H [100] zone-axis. (B-D) MoS_2 and WSe_2 are misaligned ~21° with respect to each other along the 1H [100] zone-axis. In (B) imaging is with WSe_2 in [100] zone-axis, in (C) imaging is with MoS_2 in [100] zone-axis, and in (D) imaging is with both layers far off [100] zone-axis. (**E**,**F**) STEM images of Gr/$MoSe_2$/MoS_2/WSe_2 heterostructures. In (E) $MoSe_2$, MoS_2 and WSe_2 layers are slightly misaligned with respect to each other along the 1H [100] zone-axis. In (F) all three TMD layers are approximately aligned along 1H [100] zone-axis.

Figure S2 shows cross-sectional atomic-resolution annular dark field scanning transmission electron microscopy (ADF-STEM) images of the three-layer ($Gr/MoS_2/WSe_2$) and four-layer ($Gr/MoS_2/WSe_2$) heterostructures in different samples. The monolayer graphene on top of each heterostructure is hard to discern due to the much lower atomic number of carbon atoms. In the three-layer heterostructure, atomic resolution images can be achieved for both layers when the MoS_2 and WSe_2 layers are in relatively good lattice alignment (fig. S2A). Figures S2B,C show similar, but misaligned, heterostructures when the bottom WSe_2 layer or top MoS_2 layers are imaged in [100] zone-axis, respectively. Figure S2D shows the three-layer heterostructure when all the layers are off [100] zone-axis. Figures S2E,F show the four-layer heterostructures with rough alignment of $MoSe_2$, MoS_2 and WSe_2 layers and approximately aligned all three TMD layers, respectively. We note these are all STEMs *in addition* to the ones in Fig. 1 of the main text, taken at different regions, highlighting the atomically clean and intimate nature of the interfaces.

Section S3. PL quenching in 2D heterostructures

Light emission quenching of individual monolayers in 2D heterostructures is attributed to interlayer charge transfer process due to strong interlayer coupling (*35-37*). In all our heterostructures the PL is significantly quenched with respect to the isolated monolayers, revealing intimate coupling between 2D monolayers over larger areas, and complementing the "zoomed in" view that is achievable by STEM (above). Figure S3 shows the photoluminescence (PL) spectra of isolated MoS_2 and WSe_2 monolayers, as well as Gr/MoS_2 and Gr/WSe_2 heterostructures before and after annealing. After annealing, the PL is further quenched, showing enhanced coupling due to the removal of possible water residues between the layers (*22*). In addition to PL quenching, interlayer breathing Raman modes and interlayer exciton emission can be used to confirm layer coupling in vdW heterostructures with specific system of materials and measurement set up requirements (*22,38*).

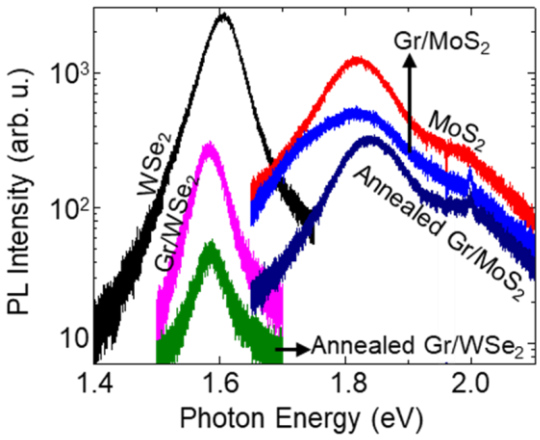

Fig. S3. PL quenching. PL spectra of isolated monolayers of MoS_2 and WSe_2, and heterostructures of Gr/MoS_2 and Gr/WSe_2 as transferred and after annealing.

Section S4. SThM thermal maps

We used scanning thermal microscopy SThM (*39*) to map the surface temperature in the heated channels with high spatial resolution (~100 nm, determined by the thermal exchange radius) (*40*). Figures S4A to H show atomic force microscopy (AFM) topography and the corresponding SThM thermal maps for graphene, Gr/MoS_2, Gr/WSe_2, and Gr/MoS_2/WSe_2 on SiO_2/Si, respectively. The SThM thermal maps reveal uniform temperature rise within the heated areas of the heterostructures. The uniform power input and temperature rise allow us to use a simple lumped thermal model to extract the thermal boundary conductance (TBC) of the interfaces of the heterostructure. The SThM voltage signal was converted to temperature using a calibration technique which is discussed in the next section.

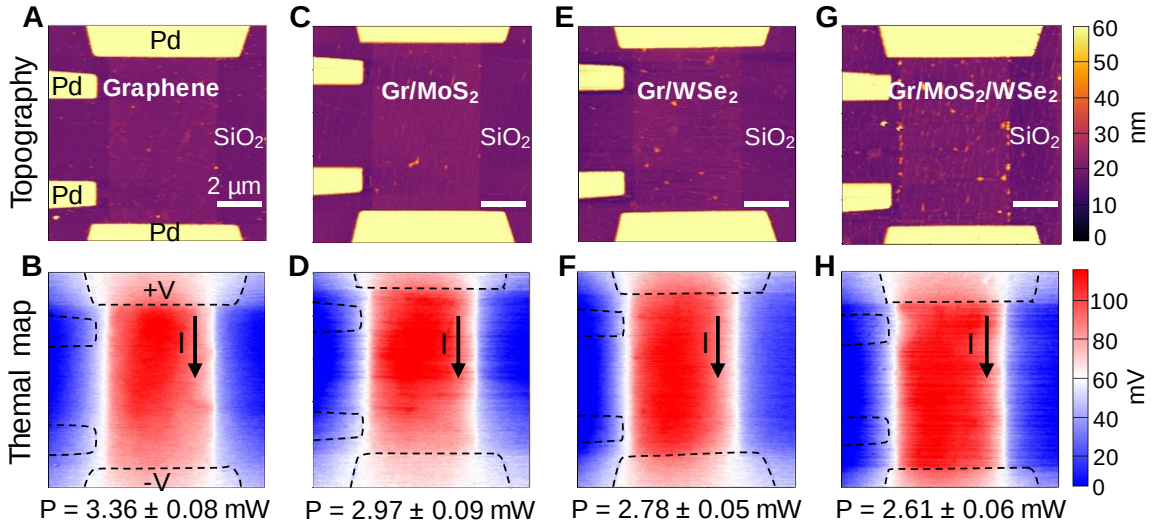

Fig. S4. Uniform heating maps. Topography and SThM thermal maps of (**A**,**B**) graphene, (**C**,**D**) Gr/MoS_2, (**E**,**F**) Gr/WSe_2 and (**G**,**H**) Gr/MoS_2/WSe_2 heterostructures, respectively. These samples were capped with 15 nm of Al_2O_3 to electrically isolate the thermal probe from the sample when biasing the device. The topography images show smooth surfaces with some non-uniformities in the Gr/WSe_2 and Gr/MoS_2/WSe_2 heterostructures. These non-uniformities are localized in small areas and correspond to bilayer/multilayer triangular islands from the WSe_2 CVD growth. The thermal maps reveal homogenous heating across the channel for the different heterostructures studied with no visible hot spots associated to the multilayer islands.

Section S5. SThM temperature calibration

To calibrate the SThM mV signal to temperature we used metal line heaters with known temperature. We fabricated 4-probe metal lines (30 nm Pd with 2 nm Ti adhesion layer) on SiO_2 (90 nm) on Si substrates with length L = 30 µm and varying width W = 100 nm to 1 µm. The

metal heaters were capped by 15 nm Al_2O_3 to keep the same thermal contact as in the graphene heater experiment. We first measured the temperature coefficient of resistance (TCR) of the Pd lines on a hot stage (fig S5A,B). With the measured TCR the temperature of the heater is given by the change in its resistance: $\Delta T = \Delta R/(R \cdot \mathrm{TCR})$. Note that the voltage drops at contacts are excluded in our 4-probe structure. We also measured the thermal resistance of the lines $\Delta T/\Delta P$. Next, the SThM tip was scanned in passive mode over the metal lines, which acted as heaters with a known temperature. Figure S5C,D shows the SThM voltage and topography of a heater with W = 1 µm. We repeated this procedure with varying input powers applied to the metal lines and calibrated the readout SThM voltage signal (in mV) to the known (heater) temperature. It should be noted that the calibration factor (K/mV) decreases for heater widths smaller than ~ 500 nm but since the graphene heaters in our experiment are wider (W = 5 µm) we used the calibration factor 7 ± 1 K/mV which we obtained for heaters wider than 500 nm (*41*).

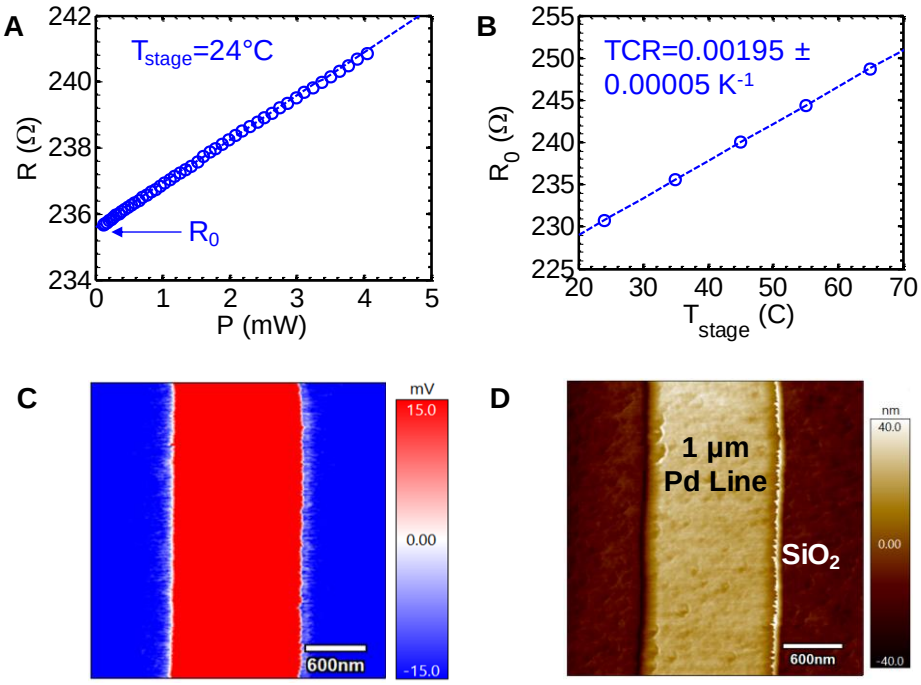

Fig. S5. SThM calibration by metal line heaters. (**A**) Representative measurement of electrical resistance vs. input power of a metal line (W = 1 µm) at 24°C showing the resistance at zero power R_0 extrapolated for P = 0. (**B**) Electrical resistance at zero power (R_0) vs. stage temperature, measured to obtain the temperature coefficient of resistance TCR = $\Delta R/(R \cdot \Delta T)$. The extracted TCR near room temperature is shown in the inset. (**C**) SThM signal (in mV) for the electrically heated metal line used for calibration. (**D**) AFM topography image of the metal line.

Section S6. Raman temperature maps

Uniform temperature maps were also obtained by Raman thermometry for each layer in the heterostructure. Figure S6A compares the conductance of a representative graphene FET and a MoS_2 FET on SiO_2 substrates measured in vacuum. Even in the on-state of the MoS_2 FET, the graphene FET has over one order of magnitude larger conductance. During Raman thermometry we applied V_G = -20 V which turns off the MoS_2 channel and all Joule heating dissipates in the graphene heater. Figures S6B,C show the Raman temperature map for an electrically heated Gr/MoS_2 channel on SiO_2/Si substrate. We follow procedures outlined in our previous work (*23*) with several modifications for the heterostructures used here (see for example sections S7 and S8 below). We note that the Raman signal is sensitive to the number of layers (*42*) and to defects (*43*), which becomes crucial when obtaining maps of the channel if the material is not entirely uniform.

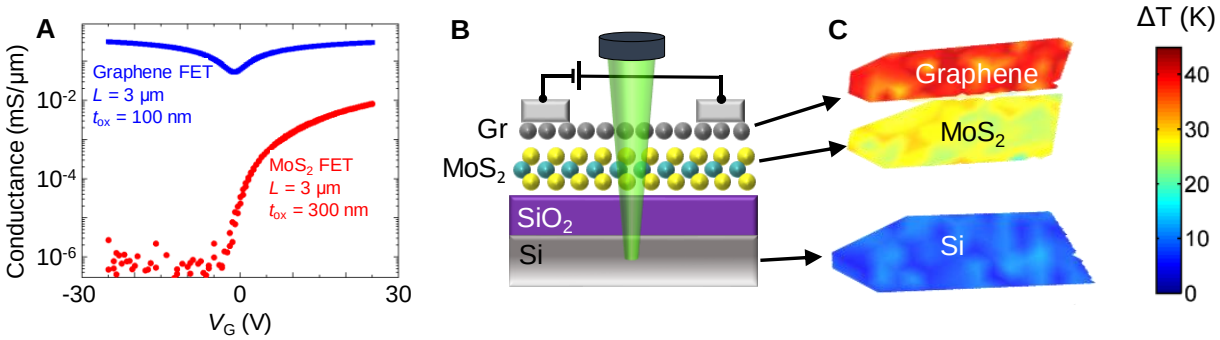

Fig. S6. Raman maps. (**A**) Normalized conductance vs. gate voltage of a representative graphene FET (on 100 nm-thick SiO_2 substrate) and an MoS_2 FET (as grown on 300 nm-SiO_2 substrate). (**B**) Schematic of the Raman thermometry experiment with Graphene/MoS_2/SiO_2/Si structure. (**C**) Map of temperature rise measured by Raman for representative device shown in B with input power of P = 7 mW. The dimensions of the graphene channel are L = 8 μm and W = 5 μm.

Section S7. Temperature-dependent Raman coefficients

For temperature-dependent Raman shift calibration, we used a Linkam THMS600 stage, and carefully differentiated effects of strain (e.g. during the calibration on hot stage) and charge (e.g. during electrical heating) (*44*), as explained in the next section.

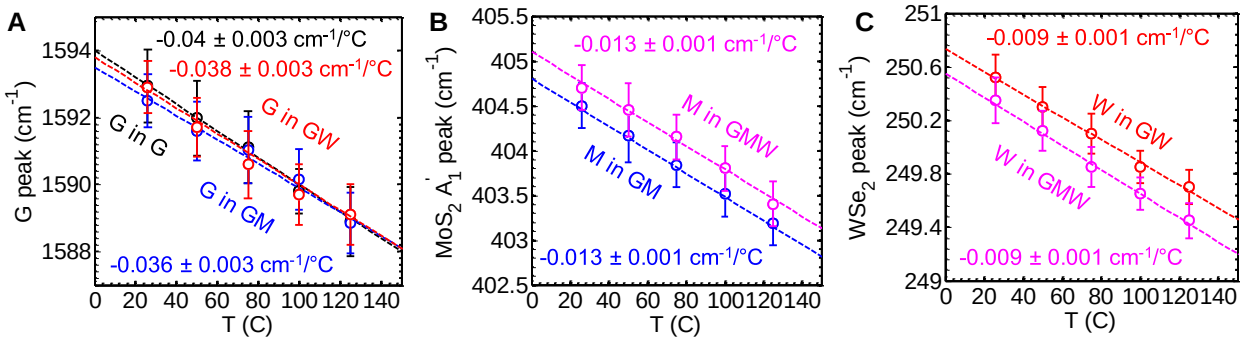

Fig. S7. Temperature-dependent Raman coefficients. (**A**) Graphene G-peak position vs. stage temperature for Gr on SiO_2/Si (G in G, black), Gr on WSe_2/SiO_2/Si (G in GW, red) and Gr on MoS_2/SiO_2/Si (G in GM, blue). All samples are capped by 15 nm Al_2O_3. (**B**) MoS_2 A_1' peak vs. stage temperature for MoS_2 in Gr/MoS_2 (M in GM, blue) and in Gr/MoS_2/WSe_2/SiO_2/Si (M in GMW, purple). (**C**) WSe_2 peak position vs. stage temperature in Gr/WSe_2/SiO_2/Si (W in GW, red) and in Gr/MoS_2/WSe_2/SiO_2/Si (W in GMW, purple).

Section S8. Non–temperature-related Raman peak shifts

8.1 Strain

The presence of strain can affect the peak position of the Raman signal which is used for the thermometry. To evaluate the effect of strain on the temperature measurements one should consider only the difference between the calibration and the electrical heating experiment. The effect of strain that may be present during the calibration procedure due to heating (of the entire sample uniformly) above room temperature will also be present during electrical heating of the same film, with one difference only due to the temperature gradient between that film and its substrate. Hence, in the evaluation of the Raman peak shifts due to such a "parasitic" strain effect, we should consider the difference in thermal expansion coefficient (TEC) between the materials and the temperature difference between the layers. The TECs of the materials in our samples and their Raman peak shifts due to strain of the 2D films are on the order of ~10^{-5} K^{-1} (*45*) roughly an order of magnitude larger than the TEC of the substrate (*46*).

The Raman peak shift with strain was measured for the MoS_2 A_1' mode as -0.4 cm^{-1} and E' mode as -2.4 cm^{-1} per 1% (*47*). For WSe_2 the peak splitting with strain was discussed (*48*) and measured (*49*) but was not quantified. We also compare the Raman shifts of the MoS_2 A_1' mode with the shifts in E' mode, which is more sensitive to strain (*47*). The Raman peak position during electrical heating (vs. input power) of the E' and A_1' peaks are shown in fig. S8A,B, and the temperature calibration of the E' mode in a representative graphene-MoS_2 sample is shown in fig. S8C. The measured thermal resistance we extract using the out-of-plane A_1' mode is 3.7 K/mW and the one that would have been extracted using the in-plane E' mode is 4.6 K/mW

(roughly ~25% larger). We assign the difference between these numbers to the effect of strain that is more dominant in the E' mode, but this result also confirms that our thermometry using the A_1' mode is insensitive to strain within the reported uncertainty, as explained next. If, for example, we assumed an extreme case for which the entire shift measured in the E' peak (~0.8 cm^{-1}) is due to strain, we would evaluate a maximum strain value < 0.4% (*47*). For the same strain value, the A_1' peak would have shifted by ~0.16 cm^{-1} which corresponds to a temperature of ~12 K, close to the uncertainty of our measurement. Given that the Raman peak shift is most likely not only due to strain, we conclude that the effect of strain on the temperature measurement using the A_1' peak in our experiment is negligible. We also note that this strain-related A_1' peak shift is (at least partially) taken into account by the hot stage calibration.

For WSe_2, no quantitative data for the peak shift with strain in monolayers are reported in literature, however based on the above discussion, and the fact that we do not observe the peak splitting in our experiment we can evaluate that the effect of strain (in electrical heating compared with stage heating) is negligible within the uncertainty of our measurement.

Finally, regarding the graphene temperature and its uncertainty, we refer to our SThM measurements (Fig. 3B) which serve as a good indication that the obtained values are within the given uncertainty.

8.2 Doping

The electrical properties and the Raman signal of the top graphene layer could be sensitive to ambient adsorbates and to the charge carrier concentration (doping). The G-peak position becomes more sensitive to charge carriers when the quasi-Fermi level is near the Dirac point (*50*). We capped the devices with ~15 nm Al_2O_3 by atomic layer deposition (ALD), which induces n-type doping and protects the graphene from the ambient. Figures S8F,G show the effect of electrostatic gating and of capping on the graphene G peak.

To eliminate the effect of charge carriers we always used the same back-gate bias V_G during electrical heating (when current I_D flows through the graphene channel) and during the reference measurement (I_D = 0, no heating). Furthermore, we carried out control measurements with large gate voltage (both positive and negative) compared with the drain voltage, so that the effective gate-to-channel bias (which varies along the channel between V_{GS} and V_{GD}) remains relatively uniform. Finally, we note that any change in carrier concentration due to temperature will be present not only during the electrical heating experiment but also during the calibration procedure and is therefore considered in our measurement.

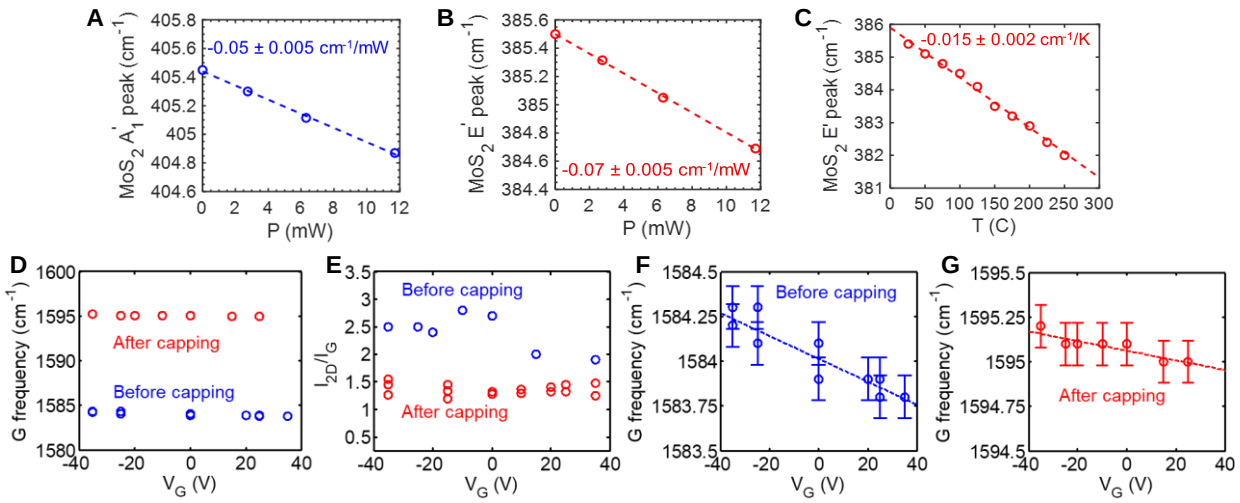

Fig. S8. Raman shift dependence on doping and electrical gating. (**A**) MoS_2 A_1' Raman peak position with input electrical power. (**B**) MoS_2 E' Raman peak position with input electrical power. (**C**) Calibration of MoS_2 E' Raman peak position with stage temperature. (**D**) Graphene G peak position vs. back-gate voltage before (blue) and after (red) capping with 15 nm Al_2O_3. (**E**) Intensity ratio of 2D (also known as G') to G peaks vs. gate voltage before and after capping. The capping layer induces a large (~10 cm^{-1}) blue-shift of the G frequency and reduction in the 2D/G intensity ratio, indicative of electron doping (*50*). (**F**) Gate voltage dependence of graphene G peak before and (**G**) after capping with Al_2O_3, zoomed in to y-axis scale of 1 cm^{-1}, highlighting more sensitivity to V_G in uncapped devices and less after capping. V_G was kept constant during the electrical heating and reference (no current) measurements to eliminate Raman shifts due to electron (or hole) electro-static doping.

Section S9. Thermal transport modeling and analysis

For 2D materials, the thermal conductance across the interface is primarily dominated by the out-of-plane or flexural phonon (ZA) modes (*32*). The dispersion for these flexural modes in 2D materials is $\omega \approx (\sigma/\rho)^{1/2}k^2$ (σ is the flexural rigidity of the 2D material, ρ is the mass density, k is the phonon wavevector) and the phonon density of states (PDOS) is given by $DOS_{ZA} = 1/[4\pi(\sigma/\rho)^{1/2}]$. The dispersion relationship for longitudinal and transverse (LA and TA) modes in SiO_2 is linear, $\omega = v_g k$, where v_g is the group velocity of the LA or TA mode, and the corresponding PDOS is $DOS_{LA,TA} = \omega^2/(2\pi^2 v_{LA,TA}^3)$. To calculate the PDOS overlap between the two materials, we also need the cut-off energies for the participating phonon branches. The active modes are calculated by obtaining the area under the curve as shown in fig. S9

$$\text{Active modes} \propto \text{PDOS overlap} \times \frac{df}{dT} \propto \int_0^{\min(\theta 1,\theta 2)} \min(DOS_1, DOS_2) \times \frac{df(\theta)}{dT}\, d\theta \qquad [S1]$$

Here, DOS_1 and DOS_2 are the PDOS for the two materials forming the interface with corresponding cut-off energies of θ_1 and θ_2 respectively. df/dT is the derivative of the Bose-Einstein distribution function with respect to temperature (T), near room temperature. The material parameters considered for the calculations are shown in table S1.

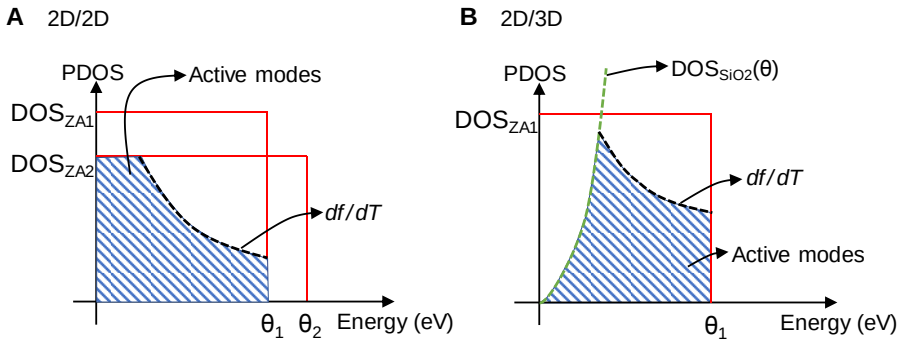

Fig. S9. PDOS overlap. Schematic representing calculation of PDOS overlap for (**A**) 2D/2D and (**B**) 2D/SiO_2 interfaces. In this figure, DOS_{ZA1} and DOS_{ZA2} are the PDOS for ZA modes of two distinct 2D materials with corresponding cut-off energies θ_1 and θ_2 respectively. For a 3D substrate such as SiO_2 we consider a PDOS from LA and TA phonon branches (DOS_{SiO2}) as shown by the green dashed line in **B**. The derivative of the Bose-Einstein distribution is shown by black dashed line. The total active modes for the respective interfaces are given by the shaded blue regions.

Table S1. Material parameters. List of material parameters used in modeling. References are listed in parentheses with gray font, after each value where appropriate.

	Flexural rigidity, σ (eV)	Mass density, ρ (g·cm^{-3})	Cut-off energy (meV)	Group velocity, v_g (m/s)	PDOS (m^{-2}s)	2D material thickness (Å)
Gr	1.1 (*51*)	2.27	60 (*52*)	-	1.65×10^5	3.35
MoS_2	9.6 (*53*)	5.06	21 (*21*)	-	1.13×10^5	6.15
WSe_2	11.45 (*54*)	9.32	15.5 (*55*)	-	1.45×10^5	6.5
SiO_2	-	2.2	20	5953 (LA) 3743 (TA) (*51*)	$\omega^2/(2\pi^2 v^3)$	-

We model the transmission at the interface using a simple acoustic mismatch model (AMM), because the interfaces of these vdW structures are nearly perfect and any surface asperities (e.g. dangling bonds) are much smaller than the phonon wavelengths. Transmission is, therefore, given by the density mismatch between the two materials.

$$\text{Trans.} \sim \min(\rho_1/\rho_2, \rho_2/\rho_1) \qquad [S2]$$

Finally, the interface TBC is proportional to the product of transmission, PDOS overlap, and df/dT, as shown in the last column of table S2 below.

Table S2. **TBC comparison.** Comparison of transmission and PDOS overlap for various interfaces.

Interfaces	Mass density mismatch (Transmission)	PDOS overlap (modes) × 10^{15}	TBC ∝ Trans. × PDOS overlap × df/dT (Normalized) [*]
Graphene/WSe_2	0.243	3.4	1
MoS_2/WSe_2	0.543	2.8	1.7
Graphene/MoS_2	0.448	3.9	1.4
Graphene/SiO_2	1.03	5.9	2.9
MoS_2/SiO_2	2.3	2.8	2.2
WSe_2/SiO_2	4.236	2.2	1.9

* This is equivalent to TBC/v_g with units of $Jm^{-3}K^{-1}$, like the specific heat. We normalize our calculations to the minimum of the Gr/WSe_2 interface. The simple model accurately captures the TBC trends found experimentally in Fig. 4, with a constant offset included for the 2D/3D interfaces, which accounts for the dimensionality mismatch. This offset originates from the fact that the underlying heat transport mechanism (phonon modes) and dimensions are different at 2D/2D and 2D/3D interfaces. Green and purple colors in the table denote 2D/2D and 2D/3D interfaces, respectively, like Fig. 4B in the main text.